ADVANCED FUNCTIONAL MATERIALS

www.afm-journal.de

Solution-Processed High-Performance Tetrathienothiophene-Based Small Molecular Blends for Ambipolar Charge Transport

Sureshraju Vegiraju, Chih-Yu Lin, Pragya Priyanka, Deng-Yi Huang, Xian-Lun Luo, Hsiang-Chi Tsai, Shao-Huan Hong, Chia-Jung Yeh, Wei-Chieh Lien, Chien-Lung Wang, Shih-Huang Tung, Cheng-Liang Liu, Ming-Chou Chen,* and Antonio Facchetti**

Four soluble dialkylated tetrathienoacene (TTAR)-based small molecular semiconductors featuring the combination of a TTAR central core, π-conjugated spacers comprising bithiophene (bT) or thiophene (T), and with/without cyanoacrylate (CA) end-capping moieties are synthesized and characterized. The molecule DbT-TTAR exhibits a promising hole mobility up to 0.36 $cm^2 V^{-1} s^{-1}$ due to the enhanced crystallinity of the microribbon-like films. Binary blends of the p-type DbT-TTAR and the n-type dicyanomethylene substituted dithienothiophene-quinoid (DTTQ-11) are investigated in terms of film morphology, microstructure, and organic field-effect transistor (OFET) performance. The data indicate that as the DbT-TTAR content in the blend film increases, the charge transport characteristics vary from unipolar (electron-only) to ambipolar and then back to unipolar (hole-only). With a 1:1 weight ratio of DbT-TTAR/DTTQ-11 in the blend, well-defined pathways for both charge carriers are achieved and resulted in ambipolar transport with high hole and electron mobilities of 0.83 and 0.37 $cm^2 V^{-1} s^{-1}$, respectively. This study provides a viable way for tuning microstructure and charge carrier transport in small molecules and their blends to achieve high-performance solution-processable OFETs.

1. Introduction

Semiconducting organic materials for organic field-effect transistors (OFETs) have received much attention due to several advantages over inorganic semiconductors, such as potential low cost, light weight, facile fabrication by solution processing as well as compatibility with large-area flexible substrates.[1–3] Small molecular semiconductors have attracted considerable interest due to the facile synthesis, easy purification, synthetic reproducibility, high purity, and well-definite molecular structure, which is very crucial for the realization of low-cost/high-performance and reproducible flexible electronics. For instance, small molecular organic semiconductors have shown excellent hole mobilities exceeding 43 $cm^2 V^{-1} s^{-1}$ in solution processed OFETs,[4–8] and exhibited power conversion efficiencies well over 10% in organic photovoltaics.[9–12] Most of the organic molecular semiconductors studied to date usually consist of π-conjugated cores bridged by donor units such as benzothiophenes (**BTs**),[13,14] dithienosiloles (**DTS**),[15,16] thienothiophenes (**TT**),[17,18] dithienothiophenes (**DTT**),[19–24] and tetrathienoacenes (**TTA**).[25–28] Among these building blocks, fused thiophenes (such as **TT**, **DTT**, and **TTA**) are attractive π-bridging units due to their strong intermolecular S···S interactions, extensive

Dr. S. Vegiraju, Dr. P. Priyanka, C.-J. Yeh, W.-C. Lien, Prof. M.-C. Chen
Department of Chemistry
National Central University
Taoyuan 32001, Taiwan
E-mail: mcchen@ncu.edu.tw

C.-Y. Lin, D.-Y. Huang, X.-L. Luo, H.-C. Tsai, S.-H. Hong, Prof. C.-L. Liu
Department of Chemical and Materials Engineering
National Central University
Taoyuan 32001, Taiwan
E-mail: clliu@ncu.edu.tw

Prof. C.-L. Wang
Department of Applied Chemistry
National Chiao Tung University
Hsinchu 30010, Taiwan

Prof. S.-H. Tung
Institute of Polymer Science and Engineering
National Taiwan University
Taipei 10617, Taiwan

Prof. A. Facchetti
Flexterra Inc.
Skokie, IL 60077, USA
E-mail: facchetti@northwestern.edu

Prof. A. Facchetti
Department of Chemistry and the Materials Research Center
Northwestern University
Evanston, IL 60208, USA

DOI: 10.1002/adfm.201801025

intramolecular π-conjugation, and close intermolecular π–π stacking. For instance, fused thiophenes exhibited hole mobilities of up to 0.05–0.42 $cm^2 V^{-1} s^{-1}$ for p-type semiconductors (molecular structures and mobilities are shown in Figure S1, Supporting Information). In contrast, benzodifurandione, naphthalenediimides (**NDI**), perylenecarboxydiimide (**PDI**), diketopyrrolopyrroles (**DPP**), perfluorophenyl, and alkyl cyanoacetates are electron-deficient π-architectures and crucial units for constructing n-type semiconductors.[29–37] For example, fluorinated **DFP-DTT** and **DFP-TTA** as well as cyanated quinoids **DTTQ** and **CMUT** exhibited high n-type carrier mobilities of 0.07–0.9 $cm^2 V^{-1} s^{-1}$ (structures and mobilities are shown in Figure S1, Supporting Information).[21,38]

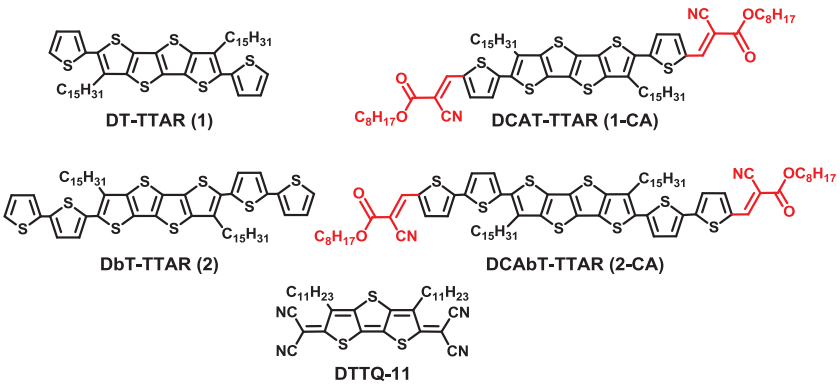

Figure 1. Chemical structures of the **TTAR**s and **DTTQ-11** semiconductors.

Ambipolar charge transport, where both types of carriers are mobile when using the appropriate bias, which are useful in certain complementary metal-oxide semiconductor logic circuits and light emitting transistors.[39,40] Although very high ambipolar mobilities were achieved for polymers,[41–45] the mobilities of small molecular ambipolar organic materials lag behind due to the difficulty in achieving the balanced energy levels to match the work function of the metal electrodes as well as induced charge instability in ambient conditions. Unlike p-type (holes from the electrode to the highest occupied molecular orbital (HOMO) level) and n-type materials (electrons from the electrode to the lowest unoccupied molecular orbital (LUMO) level), ambipolar materials must be capable of transporting both types of carriers.[46] Thus, several ambipolar semiconducting polymers could achieve proper HOMO and LUMO energies for good ambipolarity via an optimal combination of electron donor and acceptor building blocks in the polymer backbone (see Figure S2, Supporting Information). It is also worth noting that vacuum-deposited small molecule TIPS-pentacenes (**1–3**) did exhibit quite high ambipolar mobilities.[47–53] For instance, **3** exhibited a high hole mobility of 0.22 $cm^2 V^{-1} s^{-1}$ and an electron mobility up to 1.1 $cm^2 V^{-1} s^{-1}$ under vacuum. However, the electron mobility dramatically decreased to ≈10^{-3} $cm^2 V^{-1} s^{-1}$ when the devices were measured in ambient, which is attributed to its relatively high LUMO energy level of this molecule. On the other hand, solution processed ambipolar small molecules are much rare and exhibited much lower performance. For example, **BTDPP2** (Figure S2, Supporting Information) was reported with balanced hole and electron mobilities of ≈0.016 $cm^2 V^{-1} s^{-1}$, respectively.[54,55]

Tuning of the HOMO and LUMO energy levels of the same small molecule to approach to the work function of metal electrodes is not easy. Nevertheless, balanced ambipolar transport characteristics could be attained by blending well match p- and n-type organic semiconductors. As shown in Figure S3 (Supporting Information), examples of small molecular ambipolar semiconductor blends have been reported, such as blending p- and n-type pentacenes (**4–6**) resulted in ambipolar OFETs with hole and electron mobilities of 0.04 and 0.14 $cm^2 V^{-1} s^{-1}$, respectively.[56] Blending of **DHNDI:4NH2NDI**,[57] **BTBT:PDI**,[58] and **4M-DSB:CN-TFPA**[59] also achieved ambipolar characteristics with <0.06 $cm^2 V^{-1} s^{-1}$ mobilities. The quinoidal biselenophene (**QBS**) and poly(2-vinylnaphthalene) (**PVN**) blend exhibited hole and electron mobilities of 0.12 and 0.04 $cm^2 V^{-1} s^{-1}$.[60,61] Via a combination of **P-BTDT:OP-BTDT** (p-type) and C_{60} (n-type), balanced hole (0.03 $cm^2 V^{-1} s^{-1}$) and electron (0.02 $cm^2 V^{-1} s^{-1}$) mobilities were also obtained.[62] Finally, a recent study from Zhu et al reported ambipolar behavior for a donor (**DPTTA**) and acceptor (**DTTCNQ**) charge transfer complex with hole and electron mobilities of 0.77 and 0.24 $cm^2 V^{-1}s^{-1}$, respectively, for single crystal field effect transistors.[63] However, to the best of our knowledge, there is no example of solution-processed small molecule blends demonstrating balanced ambipolar characteristics with both hole and electron mobilities higher than 0.1 $cm^2 V^{-1} s^{-1}$.

In this study, a series of soluble tetrathienothiophene (**TTAR**)-based small molecules were investigated, where the **TTAR** core was connected to two thiophene (**DT**) or bithiophene (**DbT**) units to afford the p-type semiconductors **DT-TTAR** (**1**) and **DbT-TTAR** (**2**), respectively. End-functionalization of these motifs with two electron-withdrawing octyl cyanoacrylate (**CA**) moieties affords the corresponding **DCAT-TTAR** (**1-CA**) and **DCAbT-TTAR** (**2-CA**) molecules, respectively, with the goal to achieve electron-transport. The chemical structures of the four **TTAR**s are shown in **Figure 1**. The physicochemical characterizations of the four **TTAR**s were performed with $^1H/^{13}C$ NMR, differential scanning calorimetry (DSC), thermogravimetric analysis (TGA), UV–vis, and differential pulse voltammetry (DPV). Furthermore, all these compounds were investigated as semiconducting thin films for OFETs by processing with a solution-shearing method, which however demonstrates that they are all p-channel semiconductors. **DbT-TTAR** (**2**) affords the highest hole mobility of up to 0.36 $cm^2 V^{-1} s^{-1}$. Thus, next, ambipolar blends were investigated by utilization of this highest p-type performance organic semiconductor of this family and the recently developed n-type quinoidal structure **DTTQ-11**[21] as the hole and the electron-semiconductor components, respectively. The highest balanced ambipolar transport was achieved for a 1:1 weight ratio of **DbT-TTAR**:**DTTQ-11** blend composition and exhibited

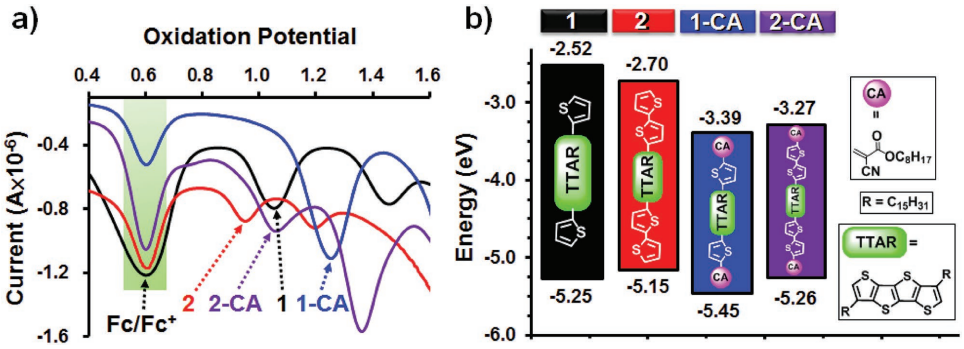

Figure 2. a) DPV curves. b) HOMO and LUMO energy levels of **1**, **2**, **1-CA,** and **2-CA** as measured in solution.

hole and electron mobilities of 0.83 and 0.37 $cm^2\ V^{-1}\ s^{-1}$, respectively. By combining optical spectroscopy, polarizing optical microscopy (POM), atomic force microscopy (AFM) and grazing incidence X-ray diffraction (GIXRD) characterizations of thin films, the aggregation, microstructure, and crystallinity of these new semiconducting films were assessed and correlated to the charge transport characteristics. To the best of our knowledge, this **DbT-TTAR**/**DTTQ-11** blend film exhibits the highest balanced ambipolar mobilities of any solution processed small molecular organic semiconductors reported to date.

2. Results and Discussion

2.1. Synthesis and Characterization

The chemical structures of the studied TTAR-based semiconductors are shown in Figure 1, and the synthetic routes are presented in Schemes S1 and S2 (Supporting Information). Thiophene and bithiophene end-capped **TTAR**s (**1-2**) are synthesized via Stille coupling of the dibrominated **TTAR** (**3**) with the corresponding stannylated thiophenes **5–6** in yields of 70–80%. The cyanoacrylate functionalized **TTAR**s (**1-CA** and **2-CA**) are prepared via Stille coupling of the distannylated **TTAR** (**4**) with the corresponding brominated cyanoacrylates **7** (41% yield) and **8** (50% yield), respectively, as shown in Scheme S1 (Supporting Information). Alternatively, **1-CA** and **2-CA** could be prepared in 75% yields via the reaction of formylated **TTAR**s **9** and **10** with the alkyl cyanoacrylate in the presence of triethylamine, as shown in Scheme S2 (Supporting Information). The formylated **9** and **10** are obtained in a 70% yield by the Stille coupling reaction of bromoformylated thiophenes (**11** and **12**, respectively) with distannylated **TTAR** (**4**). In general, the latter alternative route offers the final cyanoacrylated products in higher yields. All four compounds were characterized by conventional chemical and physical methods.

The thermal properties of these organic semiconductors were assessed using DSC and TGA (Figure S4, Supporting Information), and the corresponding thermal data is summarized in Table S1 (Supporting Information). All four compounds possess mid-high melting points (120–220 °C) with sharp endotherms above 120 °C. All compounds exhibit high thermal stability under nitrogen as measured by TGA with decomposition temperatures (5% weight loss) for all molecules >360 °C. **DbT-TTAR** (**2**) exhibits the highest thermal stability up to 400 °C.

2.2. Optical, Electrochemical, and Electronic Structure Characterization

The UV–vis absorption spectra of these molecules in *o*-dichlorobenzene and in the solid state are shown in Figure S5 (Supporting Information), which exhibit an intense and broad charge-transfer band in the UV–vis region. The optical absorption of cyanoacrylated **TTAR**s in solution exhibits a significant redshift ($\lambda_{max} \approx 500$ and 496 nm for **1-CA** and **2-CA**, respectively) relative to those of the corresponding noncyanoacrylated **TTAR**s ($\lambda_{max} \approx 390$ and 420 nm for **1** and **2**, respectively). As expected, the absorption maxima of **DbT-TTAR** (**2**) is redshifted compared to **DT-TTAR** (**1**) due to the extended conjugation in bithiophene unit. The λ_{max} of the thin films follows the same trend as the solution absorption. The absorption spectra of all thin films are broad compared to those in solutions result from solid-state intermolecular interactions, which is necessary for charge transport between the conjugated backbone. As expected, **DT-TTAR** (**1**) and **DbT-TTAR** (**2**) exhibit a larger energy gap (E_g) of 2.73 and 2.45 eV, respectively, in comparison with those of their cyanoacrylated analogues (**1-CA**; 2.06 eV and **2-CA**; 1.99 eV), determined from the thin film absorption onsets.

The electrochemical properties of the new compounds were analyzed by DPV in *o*-dichlorobenzene at 25 °C using Bu_4NPF_6 as an electrolyte. All redox potentials are referenced to ferrocene (Fc/Fc^+ was used as an internal standard calibrated at +0.60 eV). The oxidation potential curves are shown in **Figure 2**a, and the corresponding data are summarized in Table S1 (Supporting Information). The oxidation peaks of these **TTAR**s occur at +1.05 V (**1**), +0.95 V (**2**), +1.25 V (**1-CA**), and +1.06 V (**2-CA**). As expected, the oxidation potentials of the cyanoacrylated-functionalized **TTAR**s are downshifted compared to those of non cyanoacrylated analogues. The corresponding HOMO energies, estimated from the relation HOMO = $-(4.2 + E_{ox})$ are −5.25, −5.15, −5.45, and −5.26 eV for compounds **1**, **2**, **1-CA**, and **2-CA**, respectively, as shown in Figure 2b. Unsurprisingly, the HOMO energies of bithiophenyl TTARs **2** and **2-CA** are upshifted compared to those of thiophenyl analogues **1** and **1-CA**, respectively, due to the

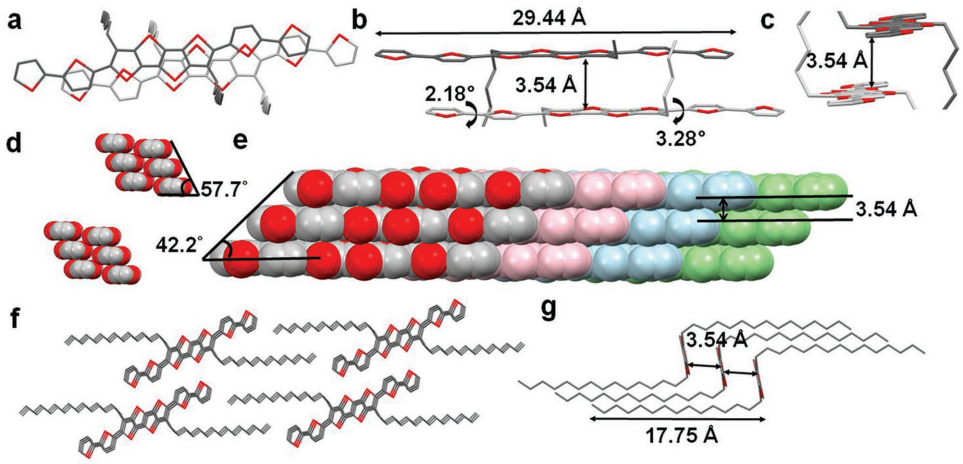

Figure 3. Crystal structure of **DbT-TTAR**, all hydrogen atoms have been omitted for the clarity. Red and black colors indicate sulfur and carbon atoms, respectively. a) Top view of two stacking **DbT-TTAR** molecules. b) Front view of two stacking **DbT-TTAR** molecules. The interplanar distance between the **DbT-TTAR** layers is ≈3.54 Å (the alkyl chains are partially omitted). c) Side view of two stacking **DbT-TTAR** molecules (the alkyl chains are partially omitted). d,e) Molecular packing arrangement of **DbT-TTAR** (the alkyl chains are omitted). f,g) Orientation of the two alkyl chains.

extended π-conjugation. The energy gap is calculated from the onset absorption from the UV–vis absorption solution spectra, accounting 2.73, 2.45, 2.06, and 1.99 eV for compounds **1**, **2**, **1-CA**, and **2-CA**, respectively. Thus, the LUMO energies of **1**, **2**, **1-CA**, and **2-CA** are found at −2.52, −2.70, −3.39, and −3.27 eV. The LUMO of the **CA**-functionalized systems are substantially deeper than the parent molecules, however, not low enough for stable electron transport in ambient.

Electronic structure calculations were performed at the B3LYP/6-31G* level of density functional theory to estimate the frontier molecular orbitals of **TTAR** compounds (Figure S6, Supporting Information). From the theoretical calculations, the HOMO and LUMO electron densities are delocalized on the whole conjugated unit for **1** and **2**. On the other hand, the HOMO electron densities of **1-CA** and **2-CA** are mostly delocalized on the **TTAR**-thiophene and **TTAR**-bithiophene units, respectively, while the LUMO is distributed on the whole molecular structure. With the introduction of alkyl cyanoacrylates as the electron withdrawing group, the calculated HOMO (−5.40 and −5.21 eV) and LUMO (−3.04 and −2.90 eV) energy levels of **1-CA** and **2-CA** are down shifted, compared to HOMO (−5.02 and −4.98 eV) and LUMO (−1.74 and −1.98 eV) of **1** and **2**, respectively. This data is fully consistent with the experimental optical absorption and DPV data.

2.3. Single Crystal Analyses of DbT-TTAR and DTTQ-11

The molecular structures of **DbT-TTAR** and **DTTQ-11**, which are used for fabricating the ambipolar blends (vide infra), were analyzed by X-Ray diffraction. Single crystals of **DbT-TTAR** were obtained by slow diffusion of methanol into a tetrahydrofuran (THF) solution of **2** (**Figure 3**). **DbT-TTAR** crystallizes in a triclinic system P-1 space group and exhibits a cofacial stacking arrangement (Figure 3d–f). The end-capped bithiophene units are almost coplanar featuring very small average torsion angles of ≈3.28° to the central tetrathienoacene core. In addition, the average dihydral angles between the two capping thiophene units are only ≈2.18°. The molecular length of **DbT-TTAR** is 29.44 Å and the interplanar distance between two **TTAR** molecules is 3.54 Å (Figure 3b,c). The cofacial stacking of **DbT-TTAR** exhibits slipping angles of 57.7° and 42.2°, as shown in Figure 3d,e. The two alkyl chains elongate in the opposite direction and are almost perpendicular to the **TTAR** core plane (Figure 3c–g). The alkyl chain length of the molecule from C1 to C15 is 17.54 Å (Figure 3g).

Single crystals of the **DTTQ-11** were obtained from slow solvent evaporation of a hexanes and dichloromethane solvent mixture. Similar to **DbT-TTAR**, **DTTQ-11** also exhibits a cofacial stacking arrangement (Figure S7a–d, Supporting Information). The two end-capped cyano methylene groups are almost coplanar to the central **DTT** core and the **DTTQs** are well connected with the neighboring molecules in a zig-zag fashion with short intermolecular S–N distances of 2.90 and 2.93 Å (Figure S7e, Supporting Information). The two alkyl chains in the **DTTQ** molecule are unsymmetically located and elongate in the same side of the **DTTQ** plane (Figure S7b–d, Supporting Information). As shown in Figure S7d (Supporting Information), one of the alkyl tails extends the first three methylene units out of the **DTTQ** core, then both alkyl tails parallel bend out of the **DTTQ** plane with a bending angle of ≈113° (Figure S7c, Supporting Information). The molecular packing of the **DTTQ** with and without the alkyl chains are shown in Figure S7c,f (Supporting Information), respectively. As shown, the interplanar distance between the two **DTTQ** molecules is quite short with an average of 3.45 Å (Figure S7b–f, Supporting Information). The planar **DTTQ** molecular structure, short packing distances, and high crystal density (1.21 g cm^{-3}) suggest ideal conditions for **DTTQ** to achieve significant electron transport in solid films.

2.4. OFETs Performance and Film Microstructure of the Pristine Semiconductors

Bottom-gate top-contact (BGTC) OFETs were first fabricated with the solution-sheared films of the pristine **TTAR**s

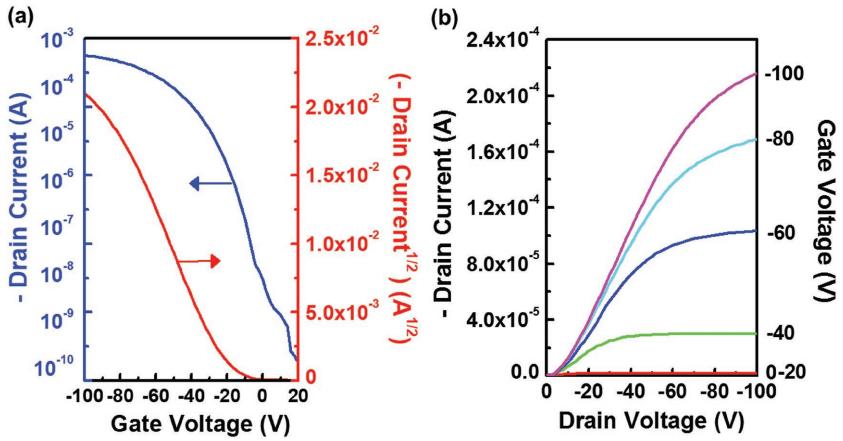

Figure 4. a) Transfer and b) output characteristic of solution-sheared OFETs based on **DbT-TTAR** thin films.

on PETS-modified Si/SiO_2 substrates. Various shearing speeds and deposition temperatures were examined to optimize the OFETs electrical performance. The thickness of the active layer was controlled at ≈50 nm. The device were completed by thermal evaporation of Au source/drain contacts (W/L = 1500/25 µm). All organic semiconductors films were solution-processed in ambient and the corresponding devices characterized both in nitrogen and ambient conditions. The average field effect mobility (μ_{avg}) was calculated using standard metal-oxide-semiconductor field-effect transistor (MOSFET) equations from the transfer characteristics of more than 10 devices in the saturation region.[64] **Figure 4** and Figures S8,S9 (Supporting Information) shows the typical transfer and output characteristics of the **TTAR** OFETs for the optimized conditions, in which the transfer curves were obtained with the drain voltage (V_d) of −100 V. All the OFET key properties of the four compounds including maximum and average mobilities (μ_{max} and μ_{avg}), threshold voltage (V_{th}), and current ON/OFF ratio (I_{ON}/I_{OFF}) are summarized in **Table 1**. Notably, despite transport measurements carried out both in inert and ambient atmospheres, all of the **TTAR**-based small molecules show only unipolar p-channel properties, the electrical performances of **DT-TTAR** are similar to those obtained previously.[26] The hole mobilities of **TTAR** compounds without the cyanoacrylate substitution (**1** and **2**) is much higher than those of the functionalized systems (**1-CA** and **2-CA**), but there are no specific trends in V_{th} and I_{ON}/I_{OFF}. Among all systems, **DbT-TTAR** showed the highest mobility of 0.36 cm^2 V^{-1} s^{-1} with a V_{th} of −16.2 ± 10.9 V and a high I_{ON}/I_{OFF} of 10^6–10^7. However, the OFET devices of the cyano-functionalized **TTAR**s (**1-CA** and **2-CA**) exhibited poor performance with a hole mobility of ≈0.001 cm^2 V^{-1} s^{-1} with a V_{th} of −22.3 ± 4.3 and −11.8 ± 4.8 V and an I_{ON}/I_{OFF} of 10^4–10^5. These data are consistent with increased hole injection barrier as well as the poor film morphologies (vide infra) of **1-CA** and **2-CA**.

The crystalline morphologies of all the solution-sheared films were investigated by POM (Figure S10, Supporting Information) and tapping-mode AFM (Figure S11, Supporting Information) techniques. The microscopic images show morphologies which consistently correlate with the device performance. Both cyano-substituted **TTAR**s (**1-CA** and **2-CA**) films deposited on the SAM-treated dielectric surface consist of small grains even though some less connected needle-like domains can be observed for the **2-CA**. Such a poor surface morphology is in good agreement with the observation that both cyanolated **TTAR**s films exhibit low OFET mobilities. When analyzing the noncyanolated **TTAR** films (**1** and **2**), continuous crystalline ribbon features of solution-sheared **2** films can be observed that increase in size to micron level but the crystalline domain size of **1** film is relatively small and discontinuous.[26] This result is also in agreement with the optical absorption data (vide infra) where more conjugated compound **2** shows a substantial bathochromic shift going from solution to the solid state (Figure S5, Supporting Information), indicating strong intermolecular interactions and aggregation. Thus, the large crystalline microribbon domains with fewer grain boundaries obtained in the solution-sheared **2** facilitate charge transport and thus enhances mobility.

2D GIXRD patterns of solution-sheared **DbT-TTAR** (Figure S12, Supporting Information) films were also recorded to elucidate the packing structures. The intense spot-like diffraction pattern indicates the formation of substantial crystalline domains. Sharp and strong (001) and (002) reflections for the **DbT-TTAR** film along the out-of-plane direction (q_z) indicates that the **DbT-TTAR** molecules tend to pack in an edge-on orientation with the long molecular axis along the direction normal to the substrates. The interlayer d_{001}-spacing of **DbT-TTAR** is 27.8 Å. This result is also consistent with the terrace height of 26.1 Å, i.e., the thickness of a single molecular stacking layer, obtained from the AFM line scan along the highlighted region of Figure S11a (Supporting Information). The considerable packing order and substantial aggregation contribute to the higher mobility of **DbT-TTAR**-based OFETs.

Table 1. Summary of OFETs parameters based on solution-sheared four **TTAR**s compounds films.

Compound	Transport type	μ_{max} [cm^2 V^{-1} s^{-1}][a)]	μ_{avg} [cm^2 V^{-1} s^{-1}][b)]	V_{th} [V][b)]	I_{ON}/I_{OFF}
DT-TTAR (1)	p	0.03	0.012 ± 0.009	−25.1 ± 6.3	10^4–10^5
DbT-TTAR (2)	p	0.36	0.14 ± 0.12	−16.2 ± 10.9	10^6–10^7
DCAT-TTAR (1-CA)	p	0.0032	0.0013 ± 0.0011	−22.3 ± 4.3	10^4–10^5
DCAbT-TTAR (2-CA)	p	0.0033	0.00091 ± 0.00086	−11.8 ± 4.8	10^4–10^5

[a)]Maximum mobility; [b)]The average TFT characteristics were obtained from more than ten devices originating from 3 to 4 semiconductor depositions.

2.5. OFET Performance and Film Microstructure of Semiconducting Blends

Most charge transport studies to date focus on solution-processed crystalline films with

a single molecular semiconductor component. However, it is of interest to investigate physical blend of binary organic semiconductors consisting of p-type and n-type materials to enable new applications or enhance the performance of ambipolar devices. For example, it is highly attractive to fabricate the OFETs with high balanced hole/electron (ambipolar) mobilities, in which the electronic channel of the heterostructured films is spatially available for charge transport within/between the binary molecules.[65,66] Thus, here we explore the mixture of p-type **DbT-TTAR** and the n-type **DTTQ-11**[21] for solution-processed ambipolar semiconducting blends in a BGTC OFET architecture. All blend films were fabricated by the solution-sheared technique (for details see the Experimental Section) and measured both in ambient and nitrogen. Note, the electrical transport measurements of these blend OFETs do not deteriorate when measured in the air due to the relatively low-lying LUMO enegy level of **DTTQ-11** (LUMO of −4.21 eV)[21] that can energetically stabilize the induced electrons.

The charge transport in **DbT-TTAR**/**DTTQ-11** blend films was investigated for blends comprising *X*% in weight of **DbT-TTAR** (X = 0, 10, 30, 50, 70, 90, 100) versus **DTTQ-11** to establish the relationship between charge carrier mobility and blend composition (**Figure 5** and data summarized in **Table 2**). It can be observed from the transfer and output curves shown in **Figure 6** and Figures S13–S16 (Supporting Information), the semiconducting blend polarity is strongly dependent on *X*%. Thus, it is found that blends with *X* = 30–70% exhibit ambipolar transport. Bicontinuous channels in this type of blend films promote the transport of positive and negative charges. Especially, the transfer curves of the blend of equal weights of p-type **DbT-TTAR** and n-type **DTTQ-11** (*X* = 50%) show the greatest ambipolar characteristics, affording very high and balanced hole/electron mobilities, μ_h/μ_e of 0.83/0.37 $cm^2\ V^{-1}\ s^{-1}$. The present mobility value is among the highest reported for p/n heterostructured films.[58,59,63,65] On the other hand, **DbT-TTAR** rich (*X* = 90%) and **DTTQ-11** rich (*X* = 10%) blend films only exhibit unipolarity with a μ_h of 0.017 $cm^2\ V^{-1}\ s^{-1}$ and a μ_e of 0.085 $cm^2\ V^{-1}\ s^{-1}$, respectively, which is in agreement with one-type of favorable charge transport between the pathway of the same compound.

Figure S17 (Supporting Information) compares the optical absorption spectra in the visible region of thin films of

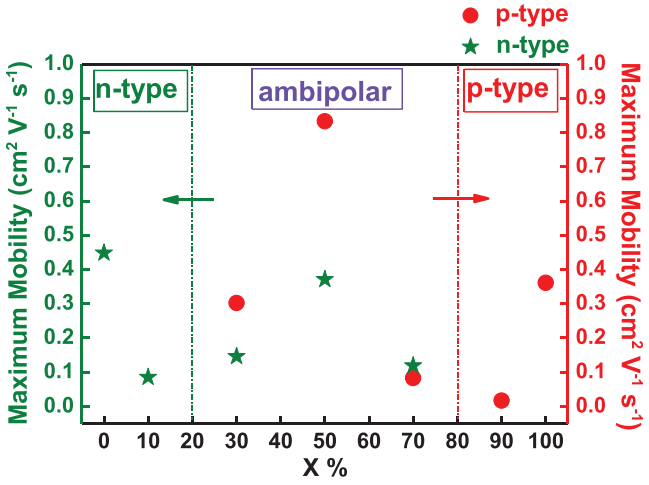

Figure 5. Maximum mobilities of blend OFETs as a function of *X*% of **DbT-TTAR**, as measured in nitrogen.

DbT-TTAR, **DTTQ-11** and their blends for various compositions. The absorption spectra of these blend films are simply the superposition of those of the neat **DbT-TTAR** and **DTTQ-11** without additional absorption peaks. As the weight fraction of **DTTQ-11** increases, the peak intensity of film at 504 nm related to **DbT-TTAR** decreases, while that of the film at 652 nm related to **DTTQ-11** increases. Furthermore, the middle absorption band slightly red-shifts from 470 to 480 nm and the shoulder peak between 500 and 600 nm becomes more pronounced. These results indicate that **DbT-TTAR** and **DTTQ-11** phase separate into primarily pure crystalline domains and retain their own structural characteristics in the blends without formation of solid solutions.

POM (**Figure 7**) and AFM (Figure S18, Supporting Information) images were used to study the film morphology of **DbT-TTAR**/**DTTQ-11** blends prepared in the same processing conditions as for OFET fabrication. POM images of both neat **DbT-TTAR** and **DTTQ-11** films show the formation of elongated microribbon strips for compositions with *X* = 30%, 50%, and 70%. However, small discontinuous crystalline grains are observed for the *X* = 10% and 90% blends. It is possible that a small amount of **DbT-TTAR** or **DTTQ-11** in these blends, respectively, may interfere with the formation of continuous

Table 2. Summary of OFETs parameters based on solution-sheared **DbT-TTAR**:**DTTQ-11** blend films.

Blend system	μ_{max} [a]		μ_{avg} [b]		V_{th} [b]	
	μ_h [$cm^2\ V^{-1}\ s^{-1}$]	μ_e [$cm^2\ V^{-1}\ s^{-1}$]	μ_h [$cm^2\ V^{-1}\ s^{-1}$]	μ_e [$cm^2\ V^{-1}\ s^{-1}$]	V_{th} (h) [V]	V_{th} (e) [V]
0%	–	0.45	–	0.29 ± 0.09	–	6.4 ± 7.0
10%	–	0.085	–	0.080 ± 0.017	–	14.2 ± 5.6
30%	0.30	0.15	0.26 ± 0.01	0.14 ± 0.02	−25.6 ± 10.8	20.1 ± 5.1
50%	0.83	0.37	0.38 ± 0.23	0.25 ± 0.06	−21.9 ± 5.3	20.8 ± 1.0
70%	0.083	0.14	0.030 ± 0.006	0.12 ± 0.02	−17.2 ± 2.0	21.3 ± 6.9
90%	0.017	–	0.014 ± 0.004	–	−16.2 ± 11.6	–
100%	0.36	–	0.14 ± 0.12	–	−16.2 ± 10.9	–

[a]Maximum mobility; [b]The average TFT characteristics were obtained from more than ten devices originating from 3 to 4 semiconductor depositions.

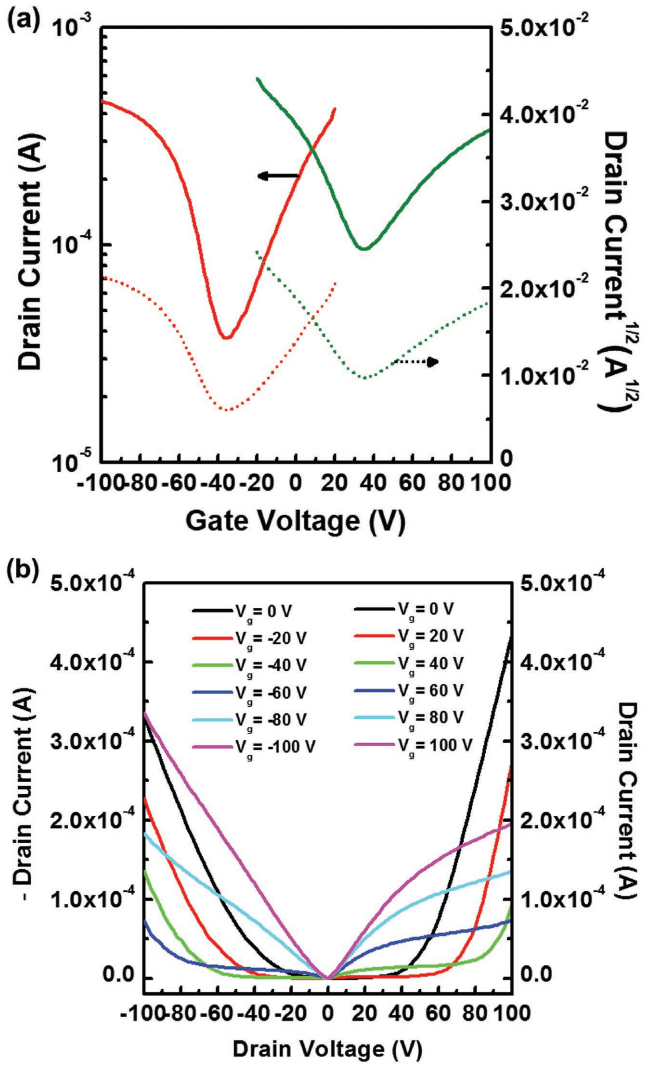

Figure 6. a) Transfer (green and red curve denote the n-channel and p-channel, respectively.) and b) output characteristic of solution-sheared OFETs based on **DbT-TTAR**/**DTTQ-11** blend thin film (X = 50%).

domains of the major component, which explains why the hole and electron mobilities of these blends are so low. When the amount of **DbT-TTAR** and **DTTQ-11** is comparable, the two components form well-defined and continuous domains acting as an effective channel for charge transport, thus enabling efficient ambipolarity.

GIXRD was conducted to obtain more structural information of pristine **DTTQ-11** and **DbT-TTAR** and their blend films (**Figure 8** and Figure S19, Supporting Information). Both GIXRD patterns of **DTTQ-11**[21] and **DbT-TTAR** reveal sharp diffraction spots originating from the (00*l*) lamella stacking along the q_z direction, suggesting the preferential edge-on stacking. The (001) peak of **DbT-TTAR** is slightly lower than that of **DTTQ-11** and the corresponding *d*-spacings for **DbT-TTAR** and **DTTQ-11** are 26.0 and 22.7 Å,[21] respectively. Upon incorporating **DbT-TTAR** into **DTTQ-11** films, the (001) peak shifts to lower q values (from 0.263 $Å^{-1}$ to 0.225 $Å^{-1}$) along the q_z direction (Figure S20, Supporting Information, the one-dimensional profile), due to the overlapping of the pristine ones. However, no additional reflections are observed for the blend films compared with those of the pristine films. Finally, as shown in Figure 8a,c, the GIXRD patterns of X = 10% and 90% blend films are basically the same as those of the **DTTQ-11** and **DbT-TTAR** films because the amounts of the minor phases are too small to be detected, further supporting the fact that unipolar n-type and p-type characteristic in these two blend systems, respectively, are due to suppression of the minority component crystallinity. The X = 50% blend film exhibits the combined diffraction patterns, as marked with red and green arrows in Figure 8b, that correspond to the diffraction from crystalline structures of the p-type semiconductor **DbT-TTAR** and n-type semiconductor **DTTQ-11**, respectively, indicating the 50% blend film can result in ambipolar characteristics through these two types of crystalline domains.

The phase transitions of **DbT-TTAR**, **DTTQ-11** and their blend (X = 50%) were further investigated by DSC. The DSC traces are displayed in Figure S21 (Supporting Information). Pure **DTTQ-11** shows three endothermic peaks on heating at 73/81 and 179 °C, which can be assigned to the crystal/liquid crystal and isotropization transitions, respectively. For pure **DbT-TTAR**, two endothermic peaks are found at 148 and 160 °C. In the case of the blended sample, multiple transitions that reveal the characteristics of both **DTTQ-11** and **DbT-TTAR** can be observed. The transitions at ≈62/75 °C and the transition at ≈143 °C are given by **DTTQ-11** and **DbT-TTAR**, respectively, implying that the two semiconductors crystallize separately in the blend. Note that the transition temperatures of the blend are lower than those of the pure samples,[67,68] which is the typical melting point depression of a crystalline substance mixed with compatible impurities. Thus, **DTTQ-11** and **DbT-TTAR** are miscible when melted. The DSC analysis supports the coexistence of crystalline phases of both materials in the blend, which can explain formation of ambipolar channels for electrons in **DTTQ-11** and holes for **DbT-TTAR** in the blend OFETs.

Finally, to better understand morphological and phase separation features of these blends, Time-of-Flight Secondary Ion Mass Spectrometry (TOF-SIMS) was carried out for the **DbT-TTAR**/**DTTQ-11** blend film with X = 50% (Figure S22, Supporting Information). The stepwise nature of the change in the Si^- signal suggests that the interface between the blend film and the bottom substrate surface is located at ≈50 nm in depth, in agreement with the blend film thickness. The signal from the secondary ions of the CN groups can be identified as a marker of **DTTQ-11**. The data shows that an even distribution of **DTTQ-11** is detected over the whole film thickness, albeit a slight prevalence of **DTTQ-11** in the middle was detected. Thus, significant vertical phase separation between the two compounds is not occurring in contrast to most small molecule–polymer blends and in other small molecule blends,[4,60,69–71] where substantial phase separation was ascribed as the source of good charge transport. Using solution-shearing film, crystal formation evolution and phase separation is different and crystallites of the two components form and grow along the shearing direction but may contribute to phase separate in the in-plane direction, which promote ambipolar charge transport with higher mobilities.

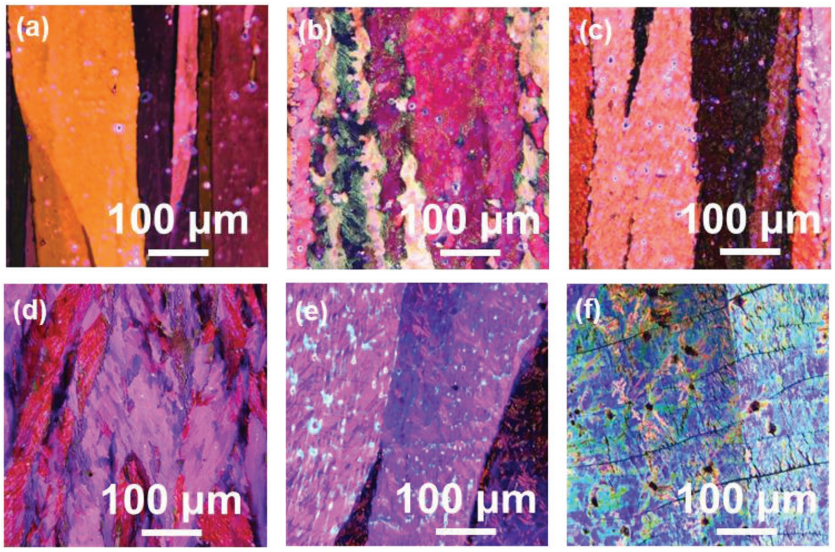

Figure 7. POM images of solution-sheared a) 0%, b) 10%, c) 30%, d) 50%, e) 70%, and f) 90% blend films.

3. Conclusions

In summary, four **TTAR**-based small molecules (with and without cyanoacrylate as end-capping moieties) were investigated for application in solution-processed OFETs. Solution-sheared **DbT-TTAR** films exhibit the highest hole mobility of up to 0.36 $cm^2 V^{-1} s^{-1}$ in this series mainly due to the stronger intermolecular interactions and increased packing ordering of the microribbon crystalline domains. Blends of p-type **DbT-TTAR** with n-type **DTTQ-11** were explored with different compositions. Unipolar charge transport was observed for the blends with a large excess of **DbT-TTAR** or **DTTQ-11**. In contrast, ambipolar charge transport was predominant for blends having 30–70% weight content of **DbT-TTAR** which is attributed to the existence of favorable crystalline phases across the channel. The best composition comprising 50% weight content of either molecule exhibits the most efficient ambipolar charge transport with maximum hole and electron mobilities of 0.83 and 0.37 $cm^2 V^{-1} s^{-1}$, respectively. These results demonstrate that molecular semiconductor blend films with proper molecules and fraction can be useful to enable solution-processed ambipolar OFETs.

4. Experimental Section

Materials: All chemicals and solvents were of reagent or anhydrous grade and were obtained from Aldrich, Alfa, and TCI Chemical Co. Solvents for reactions (toluene and THF) were distilled under nitrogen from sodium/benzophenone ketyl, and halogenated solvents were distilled from CaH_2. 3,7-dipentadecylthieno[2′,3′:4,5]thieno[3,2-b]thieno[2,3-d]thiophene (3), 2,6-di(trimethyl-stannyl)-3,7-dipentadecylthieno[3,2-b]thieno[2′,3′:4,5]thieno[2,3-d]thiophene (4), 2-bromothiophene (5), 5-bromo-2,2′-bithiophene (6), 5-bromothiophene-2-carbaldehyde (11), and 5′-bromo-[2,2′-bithiophene]-5-carbaldehyde (12) were prepared according to the procedures described in the literature.

General Synthetic Procedure for Target Compounds: Under anhydrous and deoxygenated conditions, $Pd(PPh_3)_4$ (0.05 equiv.) was added to a solution of compound (4, 1 equiv.) and monobrominated compounds (5–8; 2.3 equiv.) in dry toluene. The resulting mixture was refluxed overnight under nitrogen. After cooling to room temperature, the solvent was evaporated, the crude product was subjected to column chromatography on silica gel, and recrystallized from toluene to afford the target molecules for device fabrication.

*Synthesis of **DT-TTAR** (**1**)*: The title compound was obtained as a pale yellow solid (yield = 71%). Mp: 120 °C. ^{1}H NMR (300 MHz, $CDCl_3$): δ 7.34 (d, J = 4.8 Hz, 2 H), 7.19 (d, J = 3.6 Hz, 2 H), 7.11 (t, J = 4.4 Hz, 2 H), 2.91 (t, J = 8.1 Hz, 4 H), 1.78 (m, 4 H), 1.26 (br, 48 H), 0.88 (t, J = 6.9 Hz, 6 H). ^{13}C NMR (125 MHz, $CDCl_3$): δ 142.48, 136.32, 133.02, 132.06, 131.16, 129.37, 127.53, 126.48, 125.98, 31.94, 29.67, 29.54, 29.36, 29.07, 28.78, 22.68, 14.05. HRMS (*m*/*z*, FAB+) calcd for $C_{48}H_{68}S_6$: 836.3645, found 836.3655.

*Synthesis of **DbT-TTAR** (**2**)*: The title compound was obtained as a yellow solid (yield = 81%). Mp: 160 °C. ^{1}H NMR (300 MHz, $CDCl_3$): δ 7.41 (d, J = 5.5 Hz, 2 H), 7.36 (s, 2 H), 7.27 (d, J = 7.0 Hz, 2 H), 2.97 (t, J = 8.0 Hz, 4 H), 1.82 (m, 4 H), 1.27 (br, 48 H), 0.88 (t, J = 7.0 Hz, 6 H). ^{13}C NMR (125 MHz, $CDCl_3$): δ 142.89, 137.99, 137.15, 135.28, 133.16, 132.29, 131.16, 129.39, 128.12, 127.05, 124.89, 124.29, 124.08, 32.13, 29.89, 29.86, 29.74, 29.56, 29.25, 29.05, 22.89, 14.30. HRMS (*m*/*z*, FAB+) was calcd. for $C_{56}H_{72}S_8$ 1000.3400, and 1000.3400 was found.

*Synthesis of **DCAT-TTAR** (**1-CA**)*: After purification by column chromatography and recrystallized from acetone to afford the title compound as a purple solid (41%). Mp: 173 °C. ^{1}H NMR ($CDCl_3$; 500 MHz): δ 8.26 (s, 2 H), 7.79 (d, J = 4.0 Hz, 2 H), 7.30 (d, J = 4.0 Hz, 2 H), 4.31 (t, J = 6.5 Hz, 4 H), 3.01 (t, J = 7.2 Hz, 4 H), 1.83–1.75 (m, 8 H), 1.31–1.27 (m, 68 H), 0.90–0.88 (m, 12 H). This material was insufficiently soluble to obtain a useful ^{13}C NMR spectrum. HRMS (EI, *m*/*z*) calcd. for $C_{72}H_{102}N_2O_4S_6$ 1250.6164 (M^+). Found: 1250.6172.

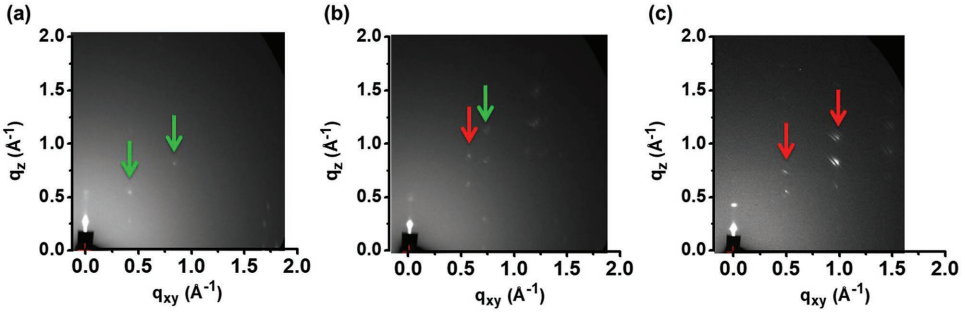

Figure 8. GIXRD images of solution-sheared blend films with X = a) 10%, b) 50%, and c) 90%. Green and red arrows denote the diffractions from **DTTQ-11** and **DbT-TTAR**, respectively.

Synthesis of ***DCAbT-TTAR (2-CA)***: After purification by column chromatography and recrystallized from acetone to afford the title compound as a purple solid in a yield of 41%. Mp: 221 °C. ^{1}H NMR ($CDCl_3$; 300 MHz):δ 8.28 (s, 2 H), 7.69 (d, J = 3.9 Hz, 2 H), 7.40 (d, J = 4.2 Hz, 2 H), 7.29 (d, J = 4.2 Hz, 2 H), 7.17 (d, J = 3.9 Hz, 2 H), 4.29 (t, J = 6.7 Hz, 4 H), 3.01 (t, J = 7.8 Hz, 4 H), 1.78–1.75 (m, 8 H), 1.24 (m, 68 H), 0.90–0.87 (m,12 H). This material was also insufficiently soluble to obtain a useful ^{13}C NMR spectrum. HRMS (EI, m/z) calcd. for $C_{80}H_{106}N_2O_4S_8$ 1414.5918 (M^++1). Found: 1415.5991.

Characterization: ^{1}H and ^{13}C NMR were recorded using a Bruker 500 or 300 instrument for all materials, with reference to solvent signals. Elemental analyses were performed on a Heraeus CHN-O-Rapid elemental analyzer. Mass spectrometric data were obtained with a JMS-700 HRMS instrument. DSC was carried out under nitrogen on a Mettler DSC 822 instrument (scanning rate of 10 °C min^{-1}). TGA was carried out using a Perkin Elmer TGA-7 thermal analysis system, using dry nitrogen as a carrier gas at a flow rate of 10 mL min^{-1} (heating rate of 10 °C min^{-1}), and reported decomposition temperatures represent the temperature observed at 5% mass loss. UV–vis absorption was carried out in the indicated solvents at room temperature with a JASCO V-530 spectrometer. DPV experiments were performed with a conventional three-electrode configuration (a platinum disk working electrode, an auxiliary platinum wire electrode, and a nonaqueous Ag reference electrode, with a supporting electrolyte of 0.1 M tetrabutylammoniumhexafluorophosphate ($TBAPF_6$) in the specified dry solvent) using a CHI621C Electrochemical Analyzer (CH Instruments). All electrochemical potentials were referenced to an Fc^+/Fc internal standard (at 0.6 V). UV–vis absorption spectroscopy measurements were conducted on a Hitachi U-4100 UV-Vis-NIR spectrophotometer. Crystallographic data (excluding structure factors) for the structure(s) reported in this paper were deposited with the Cambridge Crystallographic Data Centre as supplementary publication with the numbers CCDC 1822413 for **DbT-TTAR** and CCDC 1822414 for **DTTQ-11**. The thickness of the organic semiconductor's layer was determined by a surface profilometer (Veeco Dektak 150). Morphological observations were performed using a POM (Leica DM 2700M) connected to a Canon digital camera and AFM (Seiko SPA400) in a tapping mode at room temperature. GIXRD patterns were obtained at TLS 13A1 and 17A1 beamlines of the National Synchrotron Radiation Research Center (NSRRC) in Taiwan.

OFETs Device Fabrication and Measurement: Typical BGTC configuration was employed in the OFETs device. Heavily doped Si wafers coated with 300 nm thick SiO_2 were used as device substrates. The substrates were rinsed by ultrasonication in toluene and isopropanol, followed by drying with N_2 steam before use. The substrates were further treated by oxygen plasma for 5 min. Thereafter, the substrates were immersed in an organosilane solution in toluene (1 µL mL^{-1}) for 1 h at 55 °C, sonicated/rinsed with toluene and dried with a N_2 steam in order to form self-assembly monolayer (SAM) boned to the substrates. All the **TTAR** series compounds were dissolved in chlorobenzene or tetralin at a concentration of 2 mg mL^{-1}. For the blended OFETs, both concentrations of pristine **DbT-TTAR** and **DTTQ-11** solutions in chlorobenzene were 2 mg mL^{-1}, and then blend solutions were well-dissolved by mixing the defined mass ratios of 10:90, 30:70, 50:50, 70:30, 90:10, respectively. The solution was then deposited on the PETS-treated substrates by the solution-shearing method,[21] where the upper shearing plate (modified with ODTS) dragged the placed solution (≈20 µL) on a heated substrate (50 °C) at a controlled shearing rate of 10–20 µm s^{-1}. The fabricated films were further heated at 50 °C for 1 h under vacuum to remove residual solvent. Finally, 60 nm thick Au source/drain contact electrodes were deposited through shadow mask by thermal evaporation at a pressure of $<7 \times 10^{-7}$ Pa. The channel length and width of the OFETs were 25 and 1500 µm, respectively. Electrical characterizations of OFETs were carried out at room temperature performed in ambient air and N_2, using a Keithley 4200-SCS semiconductor parameter analyzer connected to a probe station. The mobilities (μ) and threshold voltage (V_{th}) of OFET device were extracted from the square root of the drain current (I_d) in the transfer characteristics by using the formulae of the unipolar saturated region.

Supporting Information

Supporting Information is available from the Wiley Online Library or from the author.

Acknowledgements

S.V., C.-Y.L., and P.P. contributed equally to this work. The authors acknowledge the financial support received from the Ministry of Science and Technology (MOST) of Taiwan. The authors thank Beamline B13A1/B17A1 (National Synchrotron Radiation Research Center (NSRRC) of Taiwan) for providing beamtime. The authors thank Dr. Gene-Hsiang Lee, National Taiwan University, for solving the crystal structures of the studied compounds.

Conflict of Interest

The authors declare no conflict of interest.

Keywords

ambipolar charge transport, blends, organic field-effect transistors, solution-shearing, tetrathienoacene

Received: February 7, 2018
Revised: March 29, 2018
Published online: May 21, 2018

[1] X. Guo, A. Facchetti, T. J. Marks, *Chem. Rev.* **2014**, *114*, 8943.
[2] C. Wang, H. Dong, W. Hu, Y. Liu, D. Zhu, *Chem. Rev.* **2012**, *112*, 2208.
[3] H. Dong, C. Wang, W. Hu, *Chem. Commun.* **2010**, *46*, 5211.
[4] Y. Yuan, G. Giri, A. L. Ayzner, A. P. Zoombelt, S. C. B. Mannsfeld, J. Chen, D. Nordlund, M. F. Toney, J. Huang, Z. Bao, *Nat. Commun.* **2014**, *5*, 3005.
[5] X. Yang, D. Liu, Q. Miao, *Angew. Chem., Int. Ed.* **2014**, *53*, 6786.
[6] H. Iino, T. Usui, J.-i. Hanna, *Nat. Commun.* **2015**, *6*, 6828.
[7] J. Li, Y. Zhao, H. S. Tan, Y. Guo, C.-A. Di, G. Yu, Y. Liu, M. Lin, S. H. Lim, Y. Zhou, H. Su, B. S. Ong, *Sci. Rep.* **2012**, *2*, 754.
[8] S. Vegiraju, B.-C. Chang, P. Priyanka, D.-Y. Huang, K.-Y. Wu, L.-H. Li, W.-C. Chang, Y.-Y. Lai, S.-H. Hong, B.-C. Yu, C.-L. Wang, W.-J. Chang, C.-L. Liu, M.-C. Chen, A. Facchetti, *Adv. Mater.* **2017**, *29*, 1702414.
[9] W. Zhao, S. Li, H. Yao, S. Zhang, Y. Zhang, B. Yang, J. Hou, *J. Am. Chem. Soc.* **2017**, *139*, 7148.
[10] S. j. Xu, Z. Zhou, W. Liu, Z. Zhang, F. Liu, H. Yan, X. Zhu, *Adv. Mater.* **2017**, *29*, 1704510.
[11] H. Yao, L. Ye, J. Hou, B. Jang, G. Han, Y. Cui, G. M. Su, C. Wang, B. Gao, R. Yu, H. Zhang, Y. Yi, H. Y. Woo, H. Ade, J. Hou, *Adv. Mater.* **2017**, *29*, 1700254.
[12] W. Jiang, R. Yu, Z. Liu, R. Peng, D. Mi, L. Hong, Q. Wei, J. Hou, Y. Kuang, Z. Ge, *Adv. Mater.* **2018**, *30*, 1703005.
[13] T. Mori, T. Nishimura, T. Yamamoto, I. Doi, E. Miyazaki, I. Osaka, K. Takimiya, *J. Am. Chem. Soc.* **2013**, *135*, 13900.
[14] J. Li, X. Qiao, Y. Xiong, H. Li, D. Zhu, *Chem. Mater.* **2014**, *26*, 5782.
[15] H. Usta, G. Lu, A. Facchetti, T. J. Marks, *J. Am. Chem. Soc.* **2006**, *128*, 9034.
[16] P. M. Beaujuge, W. Pisula, H. N. Tsao, S. Ellinger, K. Müllen, J. R. Reynolds, *J. Am. Chem. Soc.* **2009**, *131*, 7514.

[17] I. McCulloch, M. Heeney, C. Bailey, K. Genevicius, I. MacDonald, M. Shkunov, D. Sparrowe, S. Tierney, R. Wagner, W. Zhang, M. L. Chabinyc, R. J. Kline, M. D. McGehee, M. F. Toney, *Nat. Mater.* **2006**, *5*, 328.
[18] Y. Li, Y. Wu, P. Liu, M. Birau, H. Pan, B. S. Ong, *Adv. Mater.* **2006**, *18*, 3029.
[19] Y. M. Sun, Y. Q. Ma, Y. Q. Liu, Y. Y. Lin, Z. Y. Wang, Y. Wang, C. A. Di, K. Xiao, X. M. Chen, W. F. Qiu, B. Zhang, G. Yu, W. P. Hu, D. B. Zhu, *Adv. Funct. Mater.* **2006**, *16*, 426.
[20] M.-C. Chen, Y.-J. Chiang, C. Kim, Y.-J. Guo, S.-Y. Chen, Y.-J. Liang, Y.-W. Huang, T.-S. Hu, G.-H. Lee, A. Facchetti, T. J. Marks, *Chem. Commun.* **2009**, 1846.
[21] S. Vegiraju, G.-Y. He, C. Kim, P. Priyanka, Y.-J. Chiu, C.-W. Liu, C.-Y. Huang, J.-S. Ni, Y.-W. Wu, Z. Chen, G.-H. Lee, S.-H. Tung, C.-L. Liu, M.-C. Chen, A. Facchetti, *Adv. Funct. Mater.* **2017**, *27*, 1606761.
[22] X.-C. Li, H. Sirringhaus, F. Garnier, A. B. Holmes, S. C. Moratti, N. Feeder, W. Clegg, S. J. Teat, R. H. Friend, *J. Am. Chem. Soc.* **1998**, *120*, 2206.
[23] L. Zhang, L. Tan, Z. Wang, W. Hu, D. Zhu, *Chem. Mater.* **2009**, *21*, 1993.
[24] M.-C. Chen, S. Vegiraju, C.-M. Huang, P.-Y. Huang, K. Prabakaran, S. L. Yau, W.-C. Chen, W.-T. Peng, I. Chao, C. Kim, Y.-T. Tao, *J. Mater. Chem. C* **2014**, *2*, 8892.
[25] J. Youn, P.-Y. Huang, Y.-W. Huang, M.-C. Chen, Y.-J. Lin, H. Huang, R. P. Ortiz, C. Stern, M.-C. Chung, C.-Y. Feng, L.-H. Chen, A. Facchetti, T. J. Marks, *Adv. Funct. Mater.* **2012**, *22*, 48.
[26] S. Vegiraju, D.-Y. Huang, P. Priyanka, Y.-S. Li, X.-L. Luo, S.-H. Hong, J.-S. Ni, S.-H. Tung, C.-L. Wang, W.-C. Lien, S. L. Yau, C.-L. Liu, M.-C. Chen, *Chem. Commun.* **2017**, *53*, 5898.
[27] N. Zhou, S. Vegiraju, X. Yu, E. F. Manley, M. R. Butler, M. J. Leonardi, P. Guo, W. Zhao, Y. Hu, K. Prabakaran, R. P. H. Chang, M. A. Ratner, L. X. Chen, A. Facchetti, M.-C. Chen, T. J. Marks, *J. Mater. Chem. C.* **2015**, *3*, 8932.
[28] Y. Liu, Y. Wang, W. Wu, Y. Liu, H. Xi, L. Wang, W. Qiu, K. Lu, C. Du, G. Yu, *Adv. Funct. Mater.* **2009**, *19*, 772.
[29] J.-H. Dou, Y.-Q. Zheng, Z.-F. Yao, Z.-A. Yu, T. Lei, X. Shen, X.-Y. Luo, J. Sun, S.-D. Zhang, Y.-F. Ding, G. Han, Y. Yi, J.-Y. Wang, J. Pei, *J. Am. Chem. Soc.* **2015**, *137*, 15947.
[30] Y. Li, P. Sonar, L. Murphy, W. Hong, *Energy Environ. Sci.* **2013**, *6*, 1684.
[31] A. Facchetti, M.-H. Yoon, C. L. Stern, H. E. Katz, T. J. Marks, *Angew. Chem., Int. Ed.* **2003**, *42*, 3900.
[32] Y. Ji, C. Xiao, Q. Wang, J. Zhang, C. Li, Y. Wu, Z. Wei, X. Zhan, W. Hu, Z. Wang, R. A. J. Janssen, W. Li, *Adv. Mater.* **2016**, *28*, 943.
[33] A. Luzio, D. Fazzi, D. Natali, E. Giussani, K.-J. Baeg, Z. Chen, Y.-Y. Noh, A. Facchetti, M. Caironi, *Adv. Funct. Mater.* **2014**, *24*, 1151.
[34] M. J. Sung, A. Luzio, W.-T. Park, R. Kim, E. Gann, F. Maddalena, G. Pace, Y. Xu, D. Natali, C. de Falco, L. Dang, C. R. McNeill, M. Caironi, Y.-Y. Noh, Y.-H. Kim, *Adv. Funct. Mater.* **2016**, *26*, 4984.
[35] R. Matsidik, A. Luzio, Ö. Askin, D. Fazzi, A. Sepe, U. Steiner, H. Komber, M. Caironi, M. Sommer, *Chem. Mater.* **2017**, *29*, 5473.
[36] S. Fabiano, H. Wang, C. Piliego, C. Jaye, D. A. Fischer, Z. Chen, B. Pignataro, A. Facchetti, Y.-L. Loo, M. A. Loi, *Adv. Funct. Mater.* **2011**, *21*, 4479.
[37] G. E. Purdum, N. Yao, A. Woll, T. Gessner, R. T. Weitz, Y.-L. Loo, *Adv. Funct. Mater.* **2016**, *26*, 2357.
[38] Q. Wu, R. Li, W. Hong, H. Li, X. Gao, D. Zhu, *Chem. Mater.* **2011**, *23*, 3138.
[39] H. Sirringhaus, T. Kawase, R. H. Friend, T. Shimoda, M. Inbasekaran, W. Wu, E. P. Woo, *Science* **2000**, *290*, 2123.
[40] J. Zaumseil, H. Sirringhaus, *Chem. Rev.* **2007**, *107*, 1296.
[41] D. Khim, Y. R. Cheon, Y. Xu, W.-T. Park, S.-K. Kwon, Y.-Y. Noh, Y.-H. Kim, *Chem. Mater.* **2016**, *28*, 2287.
[42] Z. Zhao, Z. Yin, H. Chen, L. Zheng, C. Zhu, L. Zhang, S. Tan, H. Wang, Y. Guo, Q. Tang, Y. Liu, *Adv. Mater.* **2017**, *29*, 1602410.
[43] Y. Gao, X. Zhang, H. Tian, J. Zhang, D. Yan, Y. Geng, F. Wang, *Adv. Mater.* **2015**, *27*, 6753.
[44] J. Huang, Z. Mao, Z. Chen, D. Gao, C. Wei, W. Zhang, G. Yu, *Chem. Mater.* **2016**, *28*, 2209.
[45] M. Gruber, S.-H. Jung, S. Schott, D. Venkateshvaran, A. J. Kronemeijer, J. W. Andreasen, C. R. McNeill, W. W. H. Wong, M. Shahid, M. Heeney, J.-K. Lee, H. Sirringhaus, *Chem. Sci.* **2015**, *6*, 6949.
[46] S. Z. Bisri, C. Piliego, J. Gao, M. A. Loi, *Adv. Mater.* **2014**, *26*, 1176.
[47] M. L. Tang, A. D. Reichardt, N. Miyaki, R. M. Stoltenberg, Z. Bao, *J. Am. Chem. Soc.* **2008**, *130*, 6064.
[48] M. L. Tang, J. H. Oh, A. D. Reichardt, Z. Bao, *J. Am. Chem. Soc.* **2009**, *131*, 3733.
[49] M. L. Tang, A. D. Reichardt, P. Wei, Z. Bao, *J. Am. Chem. Soc.* **2009**, *131*, 5264.
[50] Z. Liang, Q. Tang, R. Mao, D. Liu, J. Xu, Q. Miao, *Adv. Mater.* **2011**, *23*, 5514.
[51] K. Zhou, H. Dong, H.-l. Zhang, W. Hu, *Phys. Chem. Chem. Phys.* **2014**, *16*, 22448.
[52] K. Szendrei, D. Jarzab, Z. Chen, A. Facchetti, M. A. Loi, *J. Mater. Chem.* **2010**, *20*, 1317.
[53] G.-J. A. H. Wetzelaer, M. Kuik, Y. Olivier, V. Lemaur, J. Cornil, S. Fabiano, M. A. Loi, P. W. M. Blom, *Phys. Rev. B* **2012**, *86*, 165203.
[54] Y. Zhang, C. Kim, J. Lin, T.-Q. Nguyen, *Adv. Funct. Mater.* **2012**, *22*, 97.
[55] H. Usta, C. Newman, Z. Chen, A. Facchetti, *Adv. Mater.* **2012**, *24*, 3678.
[56] X. Xu, T. Xiao, X. Gu, X. Yang, S. V. Kershaw, N. Zhao, J. Xu, Q. Miao, *ACS Appl. Mater. Interfaces* **2015**, *7*, 28019.
[57] X. Chen, G. Zhang, H. Luo, Y. Li, Z. Liu, D. Zhang, *J. Mater. Chem. C* **2014**, *2*, 2869.
[58] M. Treier, J.-B. Arlin, C. Ruzie, Y. H. Geerts, V. Lemaur, J. Cornil, P. Samori, *J. Mater. Chem.* **2012**, *22*, 9509.
[59] S. K. Park, S. Varghese, J. H. Kim, S.-J. Yoon, O. K. Kwon, B.-K. An, J. Gierschner, S. Y. Park, *J. Am. Chem. Soc.* **2013**, *135*, 4757.
[60] M. Kang, H. Hwang, W.-T. Park, D. Khim, J.-S. Yeo, Y. Kim, Y.-J. Kim, Y.-Y. Noh, D.-Y. Kim, *ACS Appl. Mater. Interfaces* **2017**, *9*, 2686.
[61] H. Hwang, D. Khim, J.-M. Yun, E. Jung, S.-Y. Jang, Y. H. Jang, Y.-Y. Noh, D.-Y. Kim, *Adv. Funct. Mater.* **2015**, *25*, 1146.
[62] S.-S. Cheng, P.-Y. Huang, M. Ramesh, H.-C. Chang, L.-M. Chen, C.-M. Yeh, C.-L. Fung, M.-C. Wu, C.-C. Liu, C. Kim, H.-C. Lin, M.-C. Chen, C.-W. Chu, *Adv. Funct. Mater.* **2014**, *24*, 2057.
[63] Y. Qin, J. Zhang, X. Zheng, H. Geng, G. Zhao, W. Xu, W. Hu, Z. Shuai, D. Zhu, *Adv. Mater.* **2014**, *26*, 4093.
[64] S. M. Sze, K. K. Ng, *Physics of Semiconductor Devices*, 3rd ed., John Wiley & Sons, New Jersey **2006**.
[65] J. Zhang, H. Geng, T. S. Virk, Y. Zhao, J. Tan, C.-a. Di, W. Xu, K. Singh, W. Hu, Z. Shuai, Y. Liu, D. Zhu, *Adv. Mater.* **2012**, *24*, 2603.
[66] M. Shkunov, R. Simms, M. Heeney, S. Tierney, I. McCulloch, *Adv. Mater.* **2005**, *17*, 2608.
[67] W.-B. Liau, S.-H. Tung, W.-C. Lai, L.-Y. Yang, *Polymer* **2006**, *47*, 8380.
[68] C. Müller, T. A. M. Ferenczi, M. Campoy-Quiles, J. M. Frost, D. D. C. Bradley, P. Smith, N. Stingelin-Stutzmann, J. Nelson, *Adv. Mater.* **2008**, *20*, 3510.
[69] X. Wang, W. H. Lee, G. Zhang, X. Wang, B. Kang, H. Lu, L. Qiu, K. Cho, *J. Mater. Chem. C* **2013**, *1*, 3989.
[70] K. Zhao, O. Wodo, D. Ren, H. U. Khan, M. R. Niazi, H. Hu, M. Abdelsamie, R. Li, E. Q. Li, L. Yu, B. Yan, M. M. Payne, J. Smith, J. E. Anthony, T. D. Anthopoulos, S. T. Thoroddsen, B. Ganapathysubramanian, A. Amassian, *Adv. Funct. Mater.* **2016**, *26*, 1737.
[71] N. Shin, J. Kang, L. J. Richter, V. M. Prabhu, R. J. Kline, D. A. Fischer, D. M. DeLongchamp, M. F. Toney, S. K. Satija, D. J. Gundlach, B. Purushothaman, J. E. Anthony, D. Y. Yoon, *Adv. Funct. Mater.* **2013**, *23*, 366.